# Isogrid Structural Tests and Stability Analyses

P. Slysh,* J.E. Dyer,†
*General Dynamics Convair Division, San Diego, Calif.*

J. H. Furman,‡ and J. E. Key§
*NASA Marshall Space Flight Center, Huntsville, Ala.*

**Test results and related structural instability analyses are presented for a 10-ft-diam, 37-in.-long cylinder, and a 10-ft-diam, 40 in.-long, 45-deg. conical frustum. Both structures are based upon flanged isogrids and are fabricated in 2024-T851 aluminum. Peak edge load intensities at failure were 1,654 lb/in. for the cylinder, and 1,457 lb/in. at the small diam of the frustum. General instability cylindrical-monocoque-structure equivalent knockdown factors for both were in good agreement ($\gamma = 0.48$). Design analysis is also derived for estimating critical cylinder instability edge loads from the performance of two tandem isogrid members. Evaluation is made of effective skin contributing to isogrid load-carrying cross-section.**

## Introduction

ISOGRID is an efficient grid-member and skin structure in which grid members are arranged in an isosceles triangular pattern. To use the isogrid to its maxiumum efficiency, accurate prediction of failure loads is required. Local and general instability compression failure modes are generally of primary interest. Isogrid element crippling and buckling loads can be predicted with current analytical techniques; however, as for other compression-critical structures, a wide disparity may exist between general instability failure loads predicted by theory and measured by test. It is necessary to test full-scale structural models to determine and evaluate empirical correction or "knockdown" factors that are applied to theory to predict general instability failure accurately.

This paper reviews design, development, and structural testing of flanged isogrid cylindrical and conical structures. Design equations are derived for predicting general instability and local crippling failure. These equations, as well as established isogrid design equations, are then evaluated using results of tests on full-scale isogrid structures.

Extended local instability in the cylindrical structure is evaluated with the aid of a model consisting of two tandem members having variable fixities at their ends and joining point. The model includes eccentricity accounting for anticlastic curvature or offset between load and the neutral axis. It can be used for both tensile and compressive loading. Evaluation of structural performance on the basis of this model is in agreement with results obtained using published isogrid general instability analyses.

## Cylindrical Grid Test Specimen

Figure 1 shows the test specimen, a 2024-T851 aluminum alloy flanged isogrid cylinder. The specimen is 10 ft in diam and 37 in. long. It is assembled from three panels initially machined from flat sheet and then roll formed.

Huck-bolted inside and outside splice plates (Fig. 2) create structural continuity between diagonal grid members along longitudinal panel-to-panel butt joints. Continuity between butting skins is provided by riveted splice plates. All splices are segmented to prevent hard spots in longitudinal edge stiffness.

Flanged, square-pocketed transition sections (Fig. 2) at the cylinder ends include bolted flanges and provide stiffness that spreads hard-point loading of longitudinal grid members into the bolted flange.

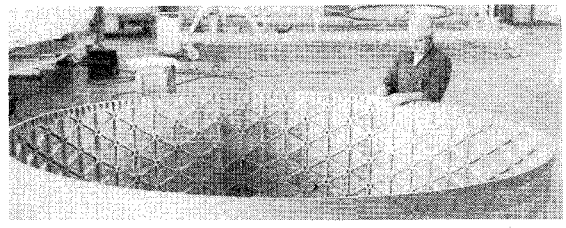

Fig. 1 Cylindrical test specimen.

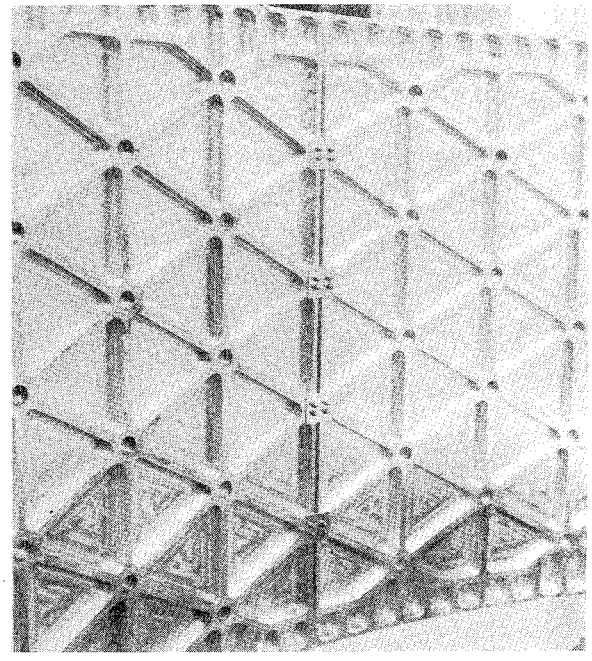

Fig. 2 Longitudinal spliced joint.

Presented as Paper 75-816 at the AIAA/ASME/SAE 16th Structures, Structural Dynamics, and Materials Conference, Denver, Colo., May 27-29, 1975; submitted June 6, 1975; revision received March 1, 1976. Work sponsored in part by NASA Contract NAS 8-29859.

Index categories: Aircraft Structural Design (including loads); LV/M Structural Design (including Loads); Structural Stability Analysis.

*Senior Design Engineer, Advanced Systems.

†Senior Structure Engineer, Structural Stress Analysis.

‡Special Assistant to Division Chief, Structural Dynamics.

§Structural Analyst, Structural Engineering Branch, Engineering Analysis Division.

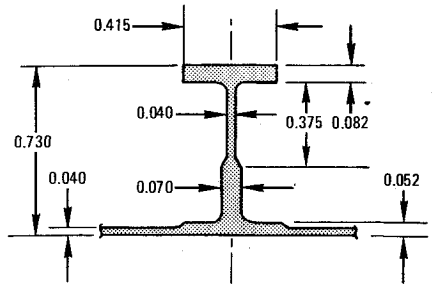


Fig. 3 Typical grid member cross-section (dimensions in inches).

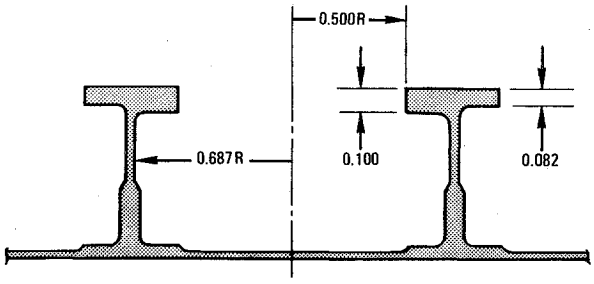


Fig. 4 Typical node cross-section (dimensions in inches).

Figure 3 is a cross-section of a typical grid member; Fig. 4 is a cross-section of a typical hollow node. Note that the inner node flange is thickened for stiffness and strength reasons.

#### Test Setup and Instrumentation

Axial and body bending loads were applied to the test specimen by two fixtures actuated by 24 hydraulic loading cylinders (numbered in Fig. 5) in which loads were measured by 24 tandem load cells. Applied flange edge load intensity was nearly proportional to the distance from the diametrical bending axis.

The test specimen was instrumented with 370 strain gages to determine grid, node, transition-section, and skin stresses, and with 160 linear transducers (having a maximum error of ±0.0003 inch) to measure radial displacements at nodes. Much of this instrumentation was concentrated in areas of expected failure. Linear transducers also measured movement between upper and lower fixtures.

#### Test Results

Test results (presented in Ref. 1 and summarized in Ref. 2) indicate that failure occurred at a peak edge load intensity of 1,654 lb/in. Figure 6 shows damage in the expected area of initial failure, about 12 in. above the lower flange. The failure was inboard and did not include nodes.

Since skins were designed to buckle elastically at about 400 lb/in., most of the applied load is reacted by grid members. At loads up to 77% of the failure load, measured forces in diagonal members were about 10% of those in longitudinal members. Just before failure, they reached 25%. This is caused by internal load redistributions resulting from local structural yielding. Grid member cross-section was assumed to include a skin width 47 times the skin thickness.

#### Structural Topography

Computer programs were developed for the CDC CYBER 70 computer and SC-4020 plotter to compute and plot test-specimen contours of radial deflections. The programs use measured radial deflections at isogrid nodes determined with the aid of linear transducers. These deflections are recorded, as is all test data, on computer data tape. Plots are drawn on a developed flat pattern of the specimen.

Topographical contours near failure load intensities (Fig. 7) indicate that the probable position of first major structural failure was either at, or more probably, 24 deg. counterclockwise from the point of nominal peak edge load intensity. This separation is explained by structural manufacturing tolerances and loading fixture flexibility. Such factors were considered in arriving at the conservative estimate of 1,654 lb/in. failure load intensity.

## Structural Analysis

Test data will be used to determine knockdown factors for a general instability model and an extended local instability model based upon two in-line longitudinal grid members.

#### General Instability

Critical edge loading for general instability is

$$N_{CRI} = \frac{\gamma}{[3(1-\nu^2)]^{1/2}} \frac{E^*(t^*)^2}{R} \tag{1}$$

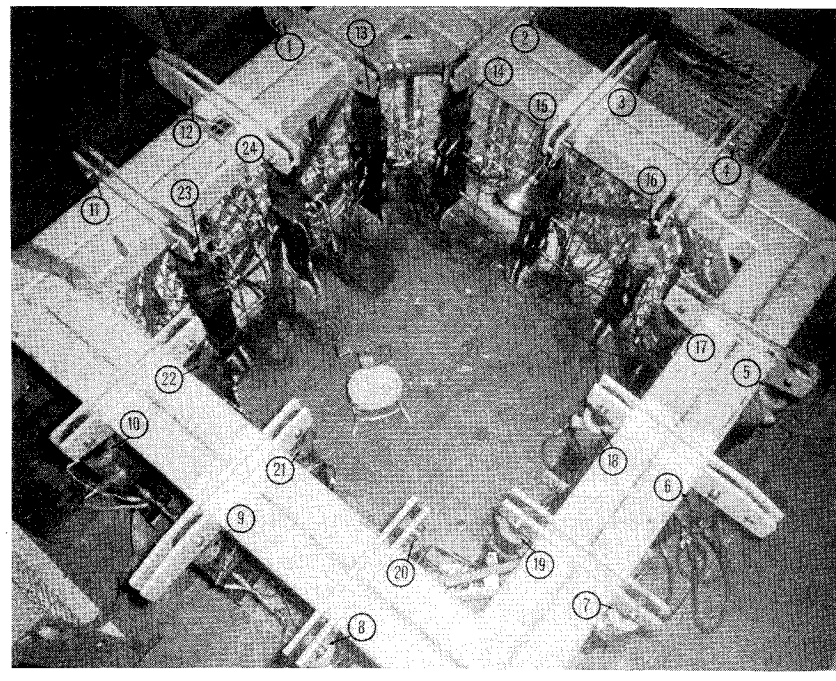

Fig. 5 Test setup.

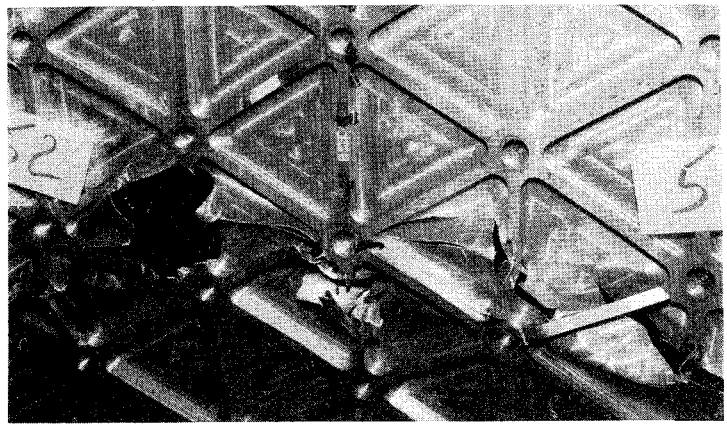

Fig. 6 Failed area of cylinder.

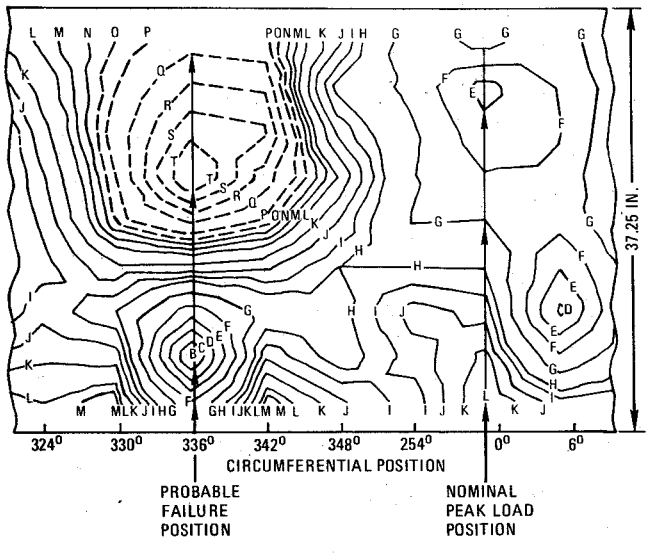


| DEFLECTION (IN.) | | | | | |
|---|---|---|---|---|---|
| B = 0.4000 | H = 0.1000 | O = −0.0100 |
| C = 0.3500 | I = 0.0800 | P = −0.0200 |
| D = 0.3000 | J = 0.0600 | Q = −0.0400 |
| E = 0.2500 | K = 0.0400 | R = −0.0600 |
| F = 0.2000 | L = 0.0200 | S = −0.0800 |
| G = 0.1500 | M = 0.0100 | T = −0.1000 |
| | N = 0.0000 | |

Fig. 7 Topographical contour near point of failure.

where

$\gamma$ = knockdown (correlation) factor

$\upsilon$ = Poisson's ratio (0.3)

$R$ = cylinder radius

$E^*$ and $T^*$ = monocoque cylinder equivalent modulus and thickness per Ref. 3.

$$E^* = E\frac{(1+\alpha+\mu)^2}{\beta}$$

$$t^* = \frac{t\beta}{1+\alpha+\mu} \tag{2}$$

where, using the symbols of Fig. 8

$$\beta^2 = (1+\alpha.\mu)\,[3(1+\delta)^2 + 3\mu(\epsilon+\lambda)^2 + 1 + \alpha\delta^2 + \mu\lambda^2] - 3[(1+\delta) - \mu(\delta+\lambda)]^2 \tag{3}$$

$$\delta = d/t, \quad \lambda = c/t, \quad \alpha = bd/th, \quad \mu = wc/th \tag{4}$$

where $h$ = height of isogrid triangle and $t$ = smeared out $t_2$ and 47 $t_1$ effective skin.

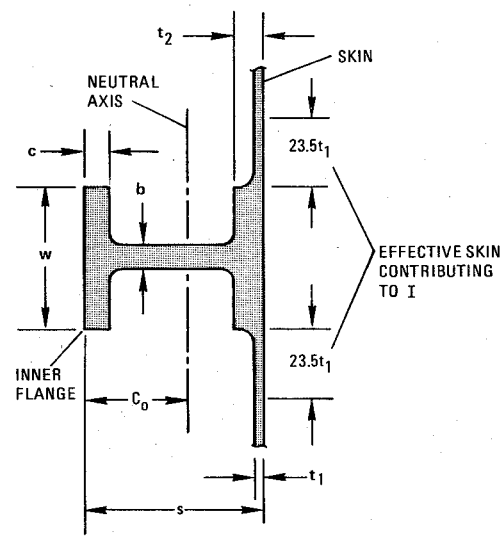


Fig. 8 Grid member cross-section.

Using R = 60 in., the cross-section in Fig. 3, and node-to-node spacing $a = 7.388$ in. in the above analysis, $\gamma = 0.48$ is computed. Figure 9 shows $N_{CR}$ vs a node-to-node spacing, for general instability, using $\gamma = 0.48$. For unbuckled skin, consistent $\gamma = .65$ was obtained in Ref. 3. Employing the analyses in Ref. 4, Fig. 9 also includes $N_{CR}$ vs "$a$" for column buckling, material yield (based upon $F_{cy} = 58{,}000$ psi), and skin buckling. Web and flange buckling-critical edge loads are greater than 4,000 lb/in. and therefore do not appear on Fig. 9. General instability is the controlling failure mode up to $a \cong 12.7$ in. in this case. As previously noted, skin buckling is not a controlling factor in load-carrying capability.

### Extended Local Instability Analysis

Beam column instabiliity of two tandem longitudinal grid members will be considered as a basis for evaluating load-carrying capability of the isogrid cylinder. That is, failure in these grid numbers is taken to trigger general instability.

### Description of Model

The model to be analyzed includes two initially straight members, the neutral axes of which intersect at a point offset $e$ with respect to a line along which applied forces $F$ act as shown in Fig. 10a. The offset is taken as positive when it is in the skin-to-inner flange direction. It can represent anticlastic or synclastic curvature, misalingment of applied forces, and eccentricity between applied forces and beam neutral axis.

A fixity due to a torsional spring rate $k_t$ is assumed to exist at Points 1 and 3 in Fig. 10. This spring rate, about a normal to grid-member plane, is determined from the model in Fig. 10b, which includes an in-line grid member of arbitrary length

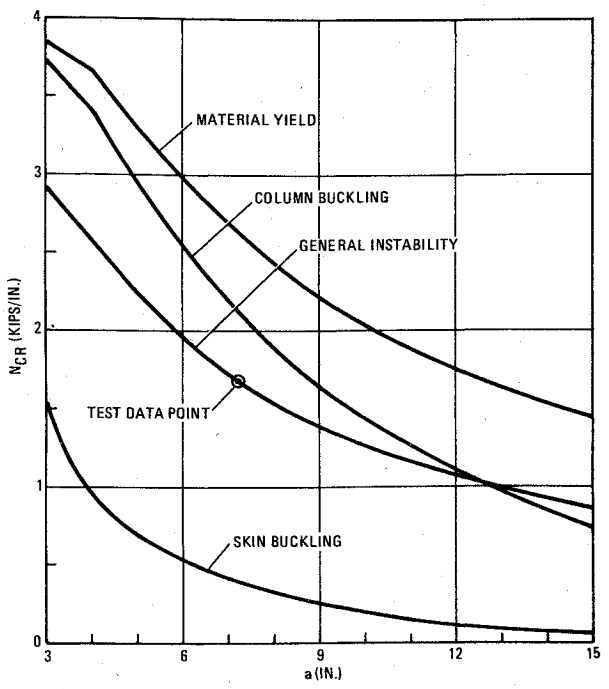


**Fig. 9 Critical edge loads vs node-to-node spacing.**

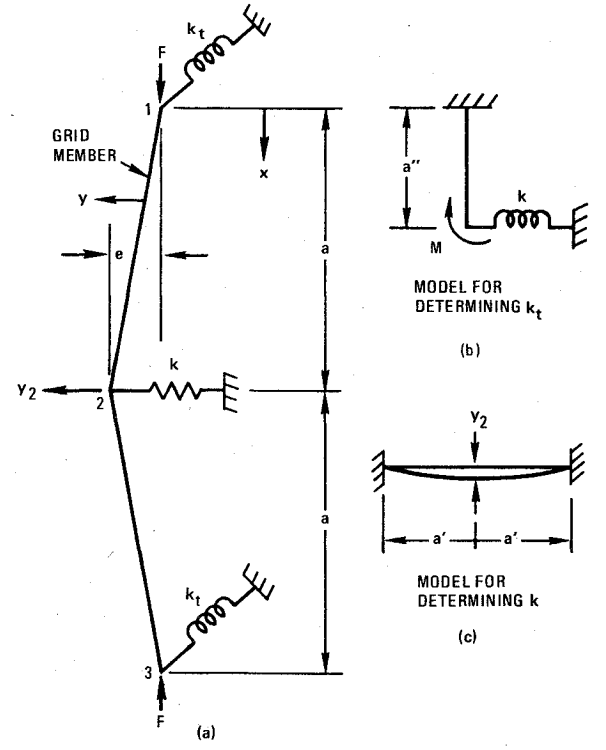


**Fig. 10 Beam column model for extended local instability analysis.**

$a''$ but having the same cross-section as isogrid grid members. Similarily, the linear spring restraint $k$ at Point 2 (also used in the model for determining $k_t$) is based on the model in Fig. 10c. An arbitrary grid member length $a'$ is used in this model. The equivalent lengths $a'$ and $a''$ are obtained from:

$$a' = K_f\, a$$
$$a'' = K_a\, a \tag{5}$$

where grid member length factors $K_f$ and $K_a$ are determined to equate theoretical and measured data.

The isogrid grid member cross-section in Fig. 8 includes 47 $t_I$ effective skin.

**Analysis**

Assuming initially a straight-line grid member between Points 1 and 2 in Fig. 10, and that $y$ is the grid member deflection with respect to this line between Points 1 and 2

$$M = -EI\, d^2y/dx^2 \tag{6}$$

where $M$, the applied bending moment, is positive when it causes compression on the right side of the grid member. $I$ is moment of inertia of section in Fig. 8. $E$ is Young's modulus.

Between Points 1 and 2:

$$M = Fy + Fex/a - k_t\Theta_1 - y_2\, kx/2 \tag{7}$$

where $\Theta_1$ is the angular deflection at Point 1 with respect to the line between Points 1 and 3, and is positive when clockwise relative to this line; $y_2$ is the displacement at Point 2 due to applied load $F$.

From Eq. (6) and (7)

$$EI\left(\frac{d^2y}{dx^2}\right) = -Fy + \left[-\frac{Fe}{a} + \frac{ky_2}{2}\right]x + k_t\Theta_1 \tag{8}$$

Eq. (8) can be modeled as:

$$\ddot{y} = b_1 y + a_1 x + c_1 \tag{9}$$

Using Laplace transorm techniques, the following solution has been developed for Eq. (9).

$$y = \left[\frac{a_1}{(-b_1)^{1.5}} + \frac{\Theta_1}{-(-b_1)^{0.5}}\right] \sin(x\sqrt{-b_1}) - \frac{a_1 x}{b_1} + \frac{c_1}{b_1}\left[\cos(x\sqrt{-b_1}) - 1\right] \tag{10}$$

This is also a solution to Eq. (8) when the following substitutions are made

$$b_1 = -F/EI \qquad b_1^I = -Fe/aEI$$
$$a_1 = b_1^I - k_{11}y_2 \qquad k_{11} = -k/2EI$$
$$c_1 = k_{14}\Theta_1 \qquad k_{14=k_t/EI} \tag{11}$$

Eq. (10) is valid when the force, $F$, is compressive and therefore $b_1$ in Eq. (11) is negative.

Slope $\Theta$ at any point on the elastic curve as a function of $x$ in given by

$$\Theta = \Theta_1 - \frac{1}{EI}\int_0^x M dx \tag{12}$$

Using Eqs. (7) and (10) in Eq. (12) and performing integration

$$\Theta = \Theta_1 + \frac{1}{EI}\left\{-F\left[\left(\frac{a_1}{(-b_1)^{1.5}} - \frac{\Theta_1}{(-b_1)^{0.5}}\right) \times \frac{\cos(x\sqrt{-b_1})}{(-b_1)^{0.5}} - \frac{1}{2}\frac{a_1 x^2}{b_1} + \frac{k_{14}\Theta_1 \sin(x\sqrt{-b_1})}{b_1(-b_1)^{0.5}} - \frac{k_{14}\Theta_1 x}{b_1}\right.\right.$$
$$\left.\left. + \left[-\frac{Fe}{a} + \frac{ky_2}{2}\right]\frac{x^2}{2} + k_t\Theta_1 x\right\} \tag{13}$$

Making use of the boundary condition $\Theta_1 = 0$ at $x = a$ in Eq. (13)

$$\Theta_1 = \frac{1}{k_2 EI}\left[-b_1' k_7 + \frac{Fea}{2} - y_2\left(\frac{ka^2}{4} - k_{11}k_7\right)\right] \tag{14}$$

where

$$k_2 = 1 - \frac{F[\cos(a\sqrt{-b_1}) - 1]}{EIb_1} + \frac{k_1 a}{EI} + \frac{k_{14}aF}{b_1 EI}$$

$$- \frac{Fk_{14}\sin(a\sqrt{-b_1})}{EIb_1(-b_1)^{0.5}} \tag{15}$$

$$k_7 = -F\left[\frac{\cos(a\sqrt{-b_1}) - 1}{b_1^2} - \frac{a^2}{2b_1}\right] \tag{16}$$

Making use in Eq. (10) of boundary condition $y = y_2$ at $x = a$ and $\Theta_1$ from Eq. (14)

$$y_2 = \frac{b_1' k_{71} + k_{72}k_{74} \div k_2 EI}{1 - k_{75}} \tag{17}$$

where

$$K_{71} = -\frac{\sin(a\sqrt{-b_1})}{(-b_1)^{1.5}} - \frac{a}{b_1}, \qquad k_{72} = -b_1' k_7 + \frac{Fea}{2} \tag{18}$$

$$k_{74} = \frac{\sin(a\sqrt{-b_1})}{(-b_1)^{0.5}} + \frac{k_{14}}{b_1}[\cos(a\sqrt{-b_1}) - 1] \tag{19}$$

$$k_{73} = \frac{ka^2}{4} - k_{11}k_7, (a\sqrt{-b_1}) - 1]$$

$$k_{75} = -k_{11}k_{71} - \frac{k_{73}k_{74}}{k_2 EI}[\exp(a\sqrt{b_1}) - \exp(-a\sqrt{b_1})] \tag{20}$$

From Eq. (17), $y_2$ is used in Eq. (14) to determine $\Theta_1$.

When the applied force is in tension, and therefore $b_1$ in Eq. (11) is positive, the sine and cosine terms in the above expressions become hyperbolic functions. Making the following substitutions, imaginary terms cancel out and solutions remain real.

$$\cos(a\sqrt{-b_1}) = \tfrac{1}{2}[\exp(a\sqrt{b_1}) + \exp(-a\sqrt{b_1})]$$

$$\sin(a\sqrt{-b_1}) = \frac{-1}{2i}[\exp(a\sqrt{b_1}) - \exp(-a\sqrt{b_1})]$$

The equivalent spring restraints $k$ and $k_t$ in Figs., 10b and 10c are

$$k = \frac{24EI}{(a')^3}, \quad k_t = \frac{EI}{a''\left[1 + \dfrac{k/4}{k/3 + EI/(a'')^3}\right]} \tag{21}$$

When $y_2$ and $\Theta_1$ are determined, $M$ can be solved from Eq. (7) and outer fiber stresses can be found from

$$S = \frac{MC_o}{I} + \frac{F}{A} \text{ or } S = \frac{M(s - C_o)}{I} + \frac{F}{A} \tag{22}$$

Maximum stresses are $S_o$ at $x = 0$ and $S_a$ at $x = a$. Analytical approach is to determine force $F$ at which $S_o$ or $S_a$ is at allowable ultimate stress $F_{tu}$ (60,000 psi). Then

$$N_{CR} = \frac{F}{(\cos 60°)\eta a} \tag{23}$$

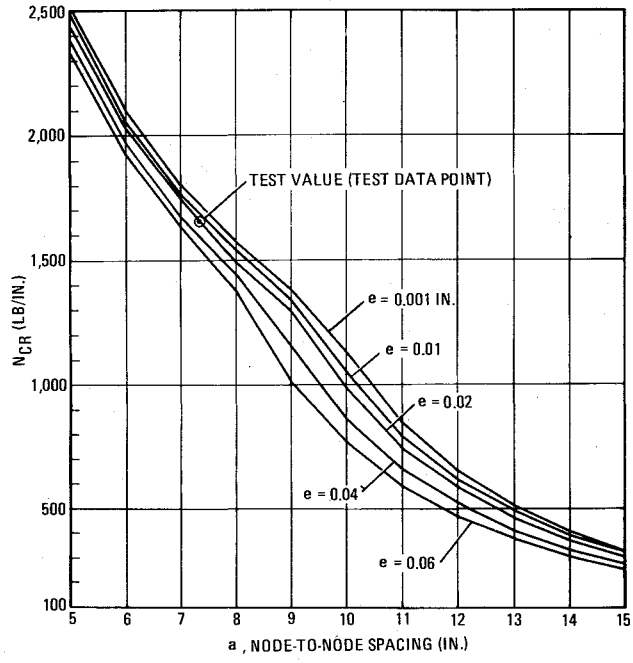


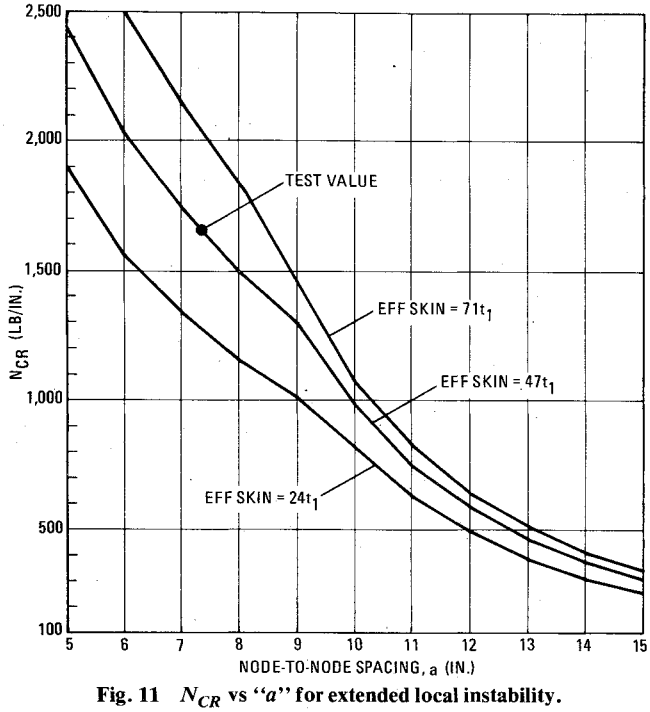


**Fig. 11 $N_{CR}$ vs "$a$" for extended local instability.**

$\eta$ = fraction of applied load reacted by longitudinal grid members (0.9 is used in this case).

### Numerical Evaluation

The above analyses were carried out using computerized iterations of $F$. It was important to dramatically reduce $F$ increments at critical loads (i.e., at $y_2 \cong 0.01a$, in this case) when $y_2$ tended to approach infinity very rapidly.

Using defined parameters and test results, the above analysis was exercised to determine $K_f = K_a = 1.4$, which produced the best test data point fit. Measured structural eccentricity $e = 0.02$ inch and $E = 10^7$ psi were used in the analysis.

Figure 11 presents $N_{CR}$ vs "$a$" for different eccentricities. Comparing Fig. 9 and 11 it is evident that extended local instability limits $N_{CR}$ for "$a$" greater than 9 in. (in this case).

At the test data point in Fig. 11, values computed in the above analysis include $y_2 \cong 0.024$, $S_o = 60{,}000$ psi, $S_a = 59{,}040$ psi, and $F \cong 9{,}400$ lb.

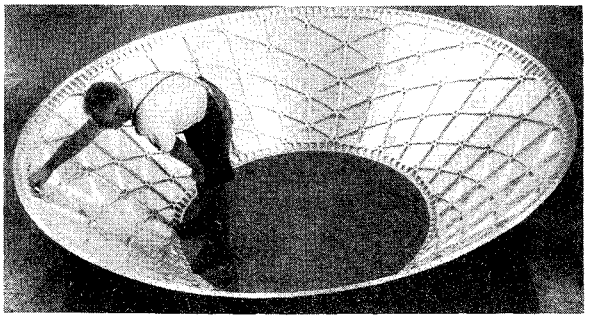

Fig. 12 Conical isogrid test specimen.

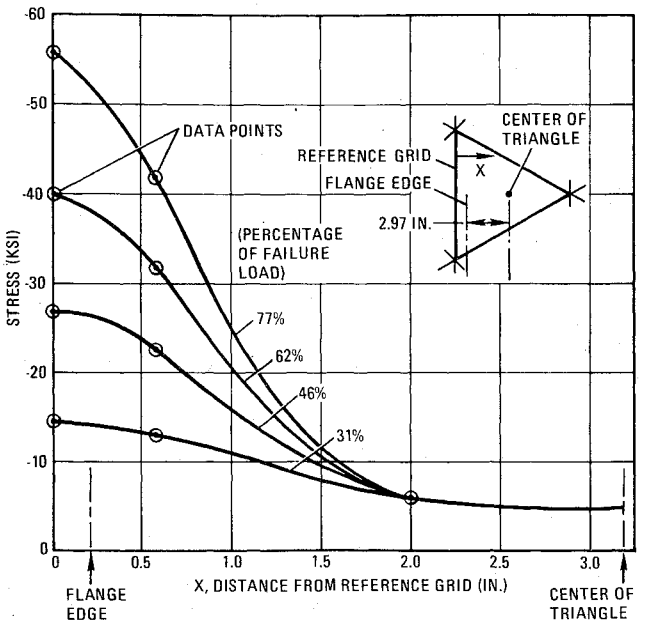


Fig. 13 Grid-skin stress distribution.

The results in Fig. 11 are based on an effective skin width of 47 $t_l$. Effects of varying these skin widths are shown in Fig. 11 where $N_{CR}$ vs $a$ is plotted for skin widths of 24 $t_l$ 47 $t_l$ and 71 $t_l$. There is no evidence that skin widths as low as 24 $t_l$ are valid. Study of load distribution in grid members at nominal peak intensity point, however, does suggest that 71 $t_l$ may be valid.

## Conical Isogrid Structure

A 10-ft-diam, 40-in.-long, 45-deg. conical frustum (Fig. 12) was tested in axial compression and body bending. The cone has diagonal grid members, described by exponential spirals, to increase grid density in approximate proportion to internally reacted edge load intensity. The grid cross-section approximates that of the isogrid cylinder previously described.

At failure, axial edge load intensities were 1,457 lb/in. at the small diameter, and 478 lb/in. at the large diameter. As in the case of the cylinder, failure was inward at about one-third the frustum length from the large diameter. At that point, the computed equivalent cylinder edge load intensity was 1,070 lb/in.

Using an analysis similar to that for the cylinder, but altered to include proportionality between $R$ and $a$, the cylinder equivalent general instability knockdown factor of $\gamma = 0.49$ was determined. This value is in good agreement with the $\gamma = 0.48$ from the cylinder test.

## Effective Skin Width

The cylindrical test specimen incorporated rosette strain gages on both sides of selected isogrid skins to determine principal skin stresses (Fig. 13) at different percentages of failure load.

Table 1 Isogrid skin panel stress

| | Percentage of Failure Load | | | |
|---|---|---|---|---|
| | 31% | 46% | 62% | 77% |
| $\sigma_{av}$ (ksi) | 8.2013 | 11.1624 | 14.0504 | 16.9290 |
| $w_{\text{eff}}$ (in.) | 1.681 | 1.231 | 1.040 | 0.901 |
| $C$ | 1.64 | 1.64 | 1.69 | 1.73 |

Effective skin width on one side of a grid member is

$$w_{\text{eff}} = 2.97\sigma_{av}/\sigma_{\text{grid}}$$

where $\sigma_{av}$ is the skin stress averaged over the 2.97 in. between the flange edge and center of isosceles triangle, and $\sigma_{\text{grid}}$ is the stress at the center of the reference grid in Fig. 13.

Using the above known values, and the following classical relationship

$$w_{\text{eff}} = C\, t_1\, E/\sigma_{\text{grid}}$$

Table 1 was derived. From Table 1, the average $C = 1.67$ is 76% greater than $C = 0.95$ for typical riveted skin-stringer construction. This difference is attributed to skin edge fixity provided by integral isogrid construction. In previous isogrid analyses, in this paper, $w_{\text{eff}} = 23.5t_l \cong 0.94$ in. was used.

## Compression Buckling of Skin

A secondary objective of the cylindrical adapter test program was to obtain test data to develop relationships for predicting compression buckling of the flanged isogrid skin panels.

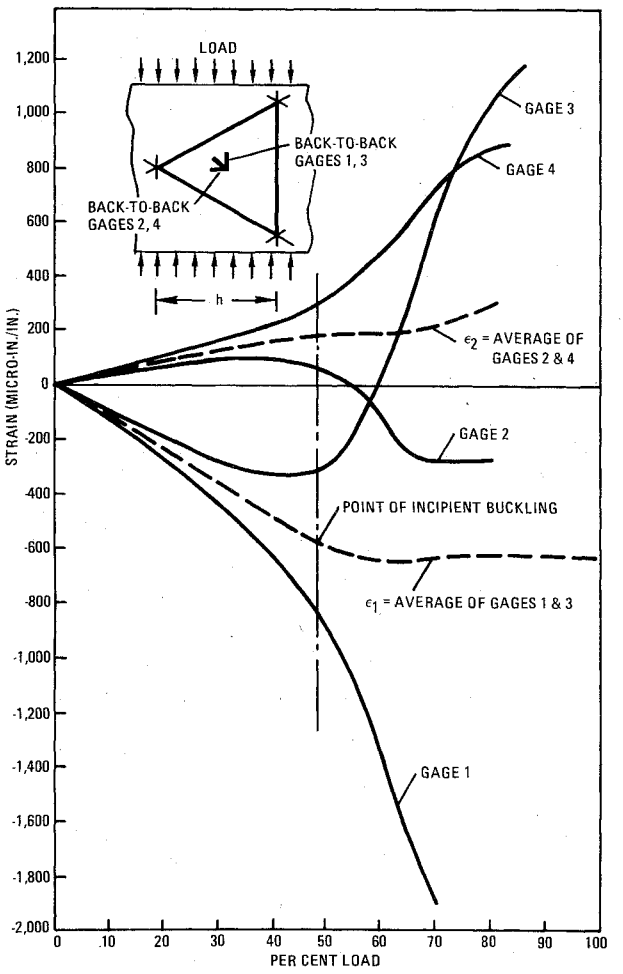


Fig. 14. Isogrid skin strain vs load.

Skin compression buckling was measured by back-to-back rosette strain gages at the center of four triangular skin panels. Typical strain data, measured parallel and perpendicular to the direction of loadings is presented in Fig. 15.

**Table 2 $K_c$ calculations for flanged isogrid test specimen**

| Panel | $t_1$ (in.) | $h$ (in.) | $\epsilon_1$ Mirco Strain | $\epsilon_2$ Mirco Strain | $\sigma_{cr}$ (psi) | $K_c$ |
|---|---|---|---|---|---|---|
| 1 | 0.039 | 6.35 | −580 | 180 | −6,069 | 16.95 |
| 2 | 0.038 | 6.35 | −550 | 240 | −5,861 | 17.25 |
| 3 | 0.037 | 6.35 | −520 | 160 | −5,446 | 16.90 |
| 4 | 0.037 | 6.35 | −520 | 150 | −5,480 | 17.00 |

$\gamma_1$ is the average strain in the direction of loading; $\epsilon_1$ is the average strain perpendicular to the direction of loading. The point of incipient buckling was defined as the point at which the $\epsilon_1$ curve in Fig. 14 starts to deviate from a straight line. The critical buckling stress is defined as

$$\sigma_{CR} = \frac{E}{1-\upsilon^2}(\epsilon_1 + \upsilon\,\epsilon_2) \tag{24}$$

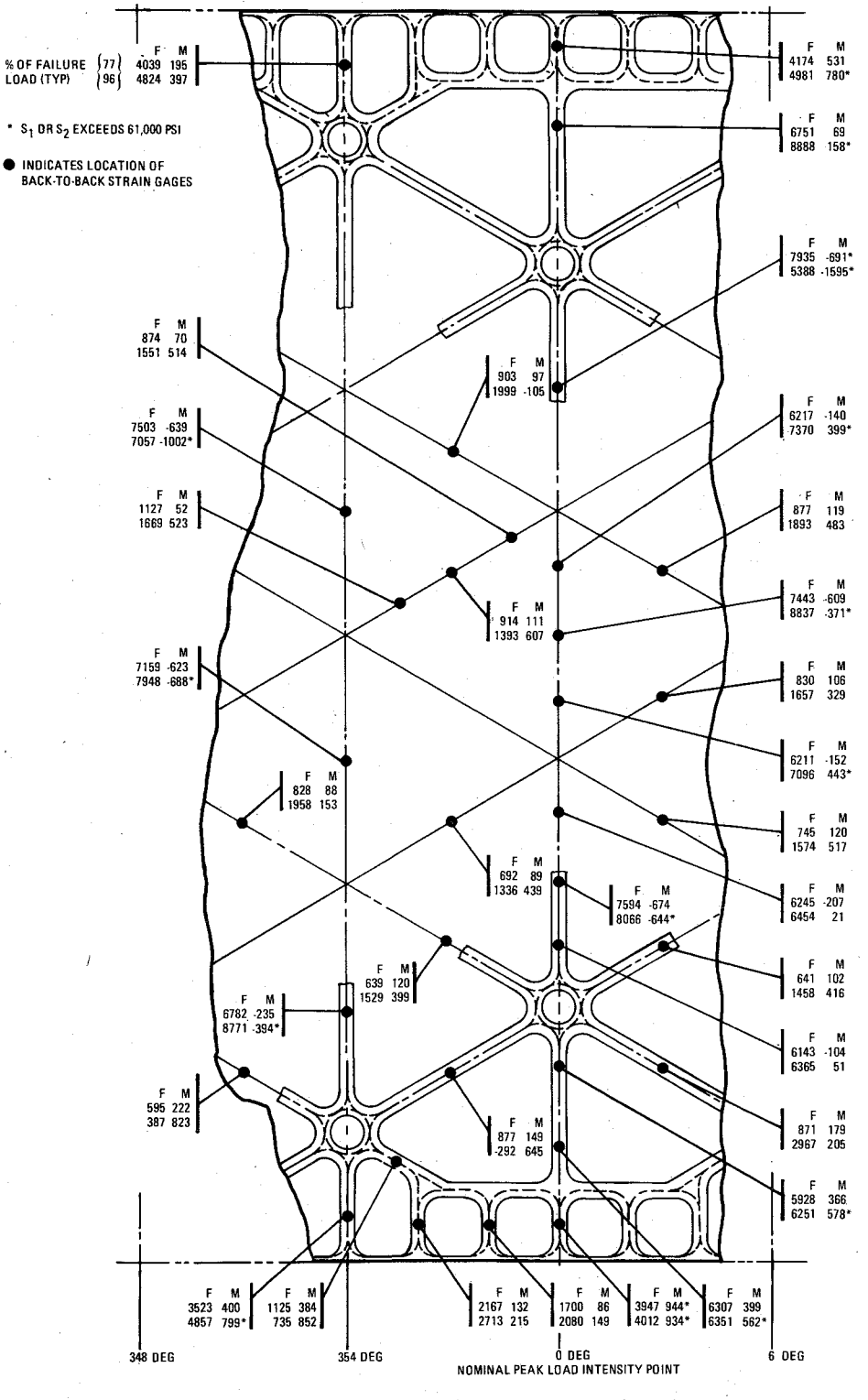


**Fig. 15 Grid member reactions near peak load intensity area.**

$\epsilon_1$ and $\epsilon_2$ being the measured strains at incipient buckling. From Ref. 5, critical buckling stress is defined as

$$\sigma CR = \frac{K_c \pi^2 E}{12(1-\nu^2)} \left[\frac{t_1}{h}\right]^2 \tag{25}$$

Solving for the buckling coefficient

$$K_c = \frac{12(1-\nu^2)\sigma_{CR}}{\pi^2 E (t_1/h)^2} \tag{26}$$

$K_c$ calculations for the four panels are summarized in Table 2. The average $K_c$ calculated for the four panels is 17.0. This value compares with $K_c = 7.5$ for triangular panels with simply supported edges and $k_c = 18.75$ for panels with clamped edges. The short, compact flanged isogrid grid members were therefore providing considerable edge fixity for the test panels.

## Reactions in Peak Load Intensity Area

In the cylindrical adapter test, the nominal peak edge load intensity point (Fig. 7) was potentially one of the places at which general instability was precipitated. It is also an area logically chosen to contain the highest strain gage concentration.

Using data from gages on inside and outside flanges, forces ($F$) and bending moments ($M$) in grid members are computed from simultaneous solution of

$$-S_1 = \frac{MC_0}{I} + \frac{F}{A} \tag{27}$$

and

$$-S_2 = \frac{M(s-C_0)}{I} + \frac{F}{A} \tag{28}$$

where $S_1$, $S_2$ are, respectively, measured stresses on the inner flange and outer flange on skin side; other symbols are as previously defined:

$C_0 = 0.504$ in., $A = 0.162$ in.$^2$, $I = 0.013$ in.$^4$, and $s = 0.73$ in.

Using the above and available $S_1$ and $S_2$, measured (strain gage) data in Eqs. (27) and (28) grid member axial forces and bending moments are computed at 77% and 96% of failure load conditions for part of the structure near the peak load intensity area. These are shown in Fig. 16. When measured stresses $S_1$ or $S_2$ exceed 61,000 psi (material ultimate stress), actual stresses are assumed to be 61,000 psi. Data in Fig. 16 are labeled with an asterisk to indicate measured stresses that exceed 61,000 psi. Negative moments imply compression in outer flange.

The following observations are made after an examination of data in Fig. 15.

1) When the structure is primarily in its elastic range (i.e., as at 77% of failure load), axial forces in the diagonal members are about 10% of axial forces in longitudinal members. At 96% of failure load, diagonal members experience as much as 25% of the load in longitudinal members. This is caused by load redistributions due to local yielding in the structure.

2) Positive moments in transition structure grid members at the upper and lower bolted flanges indicates possible failure of jack bolts in flanges of loading fixture (i.e., the loading fixture flanges were equipped with jack bolts for prying flanges to induce edge moments in addition to line loads, but these were set for no prying action during the final load to failure test). This loading flange failure caused load to be relieved from the skin side of the structure and to be picked up on the inboard side of the loading fixture flange. The high bending moment in the failed longitudinal grid members may have precipitated overall failure by failing inner flanges alternatively in compression and tension. The negative bending moment in the failed grid member at 354 deg is due to beam column effect, while at 0 deg it is due to flange kick moments.

3) Shear flow in skins and loads in diagonal members accounts for variations in loads along longitudinal members.

4) Since diagonal grid members experience less load than in-line grid members, it may be reasonable to assume that an effective skin width greater than the 47 $t_1$ should be used in computing the cross-sectional properties of diagonal members. If 70 $t_1$ were assumed, loads in the diagonal members would be greater than those indicated in Fig. 17 by about 17%, which are significant compared to loads in longitudinal grid members.

## Summary of Results

Smeared-out structure equivalent knockdown (correlation) factor $\gamma = .48$ is determined for tested flanges isogrid cylindrical and conical structures. Grid member length factors $K_f = K_a = 1.4$ are estimated in an extended local instability analysis to relate the failure of two tandem grid members to general instability. Skin buckling coefficient $K_c = 17$ is computed from experimental data.

## References

[1] Hildebrand, A. G., "Isogrid Cylinder Structural Test," NASA Marshall Space Flight Center Report IN – ETI3-74-1, 1974.

[2] Slysh, P. and Dyer, J. E., "Conical Isogrid Structural Test Program," NASA Marshall Space Flight Center, Report CR-120205,

[3] *Isogrid Design Handbook,* NASA Marshall Space Flight Center, Report, CR-124075, Feb. 1973.

[4] Slysh, P., Ringwald, R. S., Dyer, J. E., and Browning, D. L., "Isogrid Weight Optimum Structures," Paper 1063, presented at 34th Annual Conference on Mass Properties Engineering, Society of Allied Weight Engineers, Seattle, Wash. May 5-7, 1975.

[5] Timoshenko, S. P. and Woinowsky-Krieger, S., *Theory of Plates and Shells,* McGraw Hill, 1959.